

ALMA Detection of Bipolar Outflows: Evidence for Low Mass Star Formation within 1pc of Sgr A*

F. Yusef-Zadeh¹, M. Wardle², D. Kunneriath³, M. Royster¹, A. Wootten³ & D. A. Roberts⁴

¹*CIERA, Department of Physics and Astronomy Northwestern University, Evanston, IL
60208*

²*Dept of Physics and Astronomy, Research Centre for Astronomy, Astrophysics
and Astrophotonics, Macquarie University, Sydney NSW 2109, Australia*

³*National Radio Astronomy Observatory, Charlottesville, VA 22903*

⁴*Fort Worth Museum of Science and History, Fort Worth, TX 76107*

ABSTRACT

We report the discovery of 11 bipolar outflows within a projected distance of 1pc from Sgr A* based on deep ALMA observations of ¹³CO, H30 α and SiO (5-4) lines with sub-arcsecond and $\sim 1.3 \text{ km s}^{-1}$ resolutions. These unambiguous signatures of young protostars manifest as approaching and receding lobes of dense gas swept up by the jets created during the formation and early evolution of stars. The lobe masses and momentum transfer rates are consistent with young protostellar outflows found throughout the disk of the Galaxy. The mean dynamical age of the outflow population is estimated to be $6.5_{-3.6}^{+8.1} \times 10^3$ years. The rate of star formation is $\sim 5 \times 10^{-4} M_{\odot} \text{ yr}^{-1}$ assuming a mean stellar mass of $\sim 0.3 M_{\odot}$. This discovery provides evidence that star formation is taking place within clouds surprisingly close to Sgr A*, perhaps due to events that compress the host cloud, creating condensations with sufficient self-gravity to resist tidal disruption by Sgr A*. Low-mass star formation over the past few billion years at this level would contribute significantly to the stellar mass budget in the central few pc of the Galaxy. The presence of many dense clumps of molecular material within 1pc of Sgr A* suggests that star formation could take place in the immediate vicinity of supermassive black holes in the nuclei of external galaxies.

Subject headings: accretion, accretion disks — black hole physics — Galaxy: center

1. Introduction

The $4 \times 10^6 M_\odot$ black hole at the center of the Milky Way, Sgr A*, is expected to suppress star formation in nearby interstellar clouds because of tidal disruption by the black hole’s gravitational field (Morris 1993). Nevertheless, objects resembling dust-enshrouded young stars (Eckart et al. 2004; Yoshikawa et al. 2013; Yusef-Zadeh et al. 2015b) and photo-evaporative flows from their disks (Yusef-Zadeh et al. 2015b, 2016) have been identified within a few light years of Sgr A*. Clear identification of the nature of these objects has been hampered by the Galactic center’s distance, 30 magnitudes of foreground extinction, and stellar crowding.

The density required for self-gravity to overcome the tidal field of Sgr A*, $\sim 10^7 (r/\text{pc})^{-3} \text{ cm}^{-3}$, far exceeds the density in molecular clouds ($\lesssim 10^6 \text{ cm}^{-3}$) and so is believed to inhibit star formation via gravitational collapse of dense regions of clouds. By contrast, the concentration of ~ 100 OB stars within $\sim 0.4 \text{ pc}$ ($\sim 10''$) of Sgr A* (Eckart et al. 2004; Paumard et al. 2006; Lu et al. 2009) is a few million years old, and is thought to have formed in its present disk-like geometry. Approximately seven to eight million years ago, a migrating molecular cloud swept past Sgr A* and captured material forming a gaseous disk orbiting Sgr A* (Nayakshin et al. 2007; Wardle & Yusef-Zadeh 2008, 2012; Bonnell & Rice 2008; Mapelli et al. 2012). The disk became gravitationally unstable as it settled and cooled, and fragmented into stars.

A variety of observations suggest that star formation is happening inside clouds within a parsec of Sgr A* despite inhibition by tidal disruption. These include compact sources suggestive of embedded young stars (Eckart et al. 2004, 2013; Yoshikawa et al. 2013; Yusef-Zadeh et al. 2015a) and their precursor dense cloud cores (Tsuboi et al. 2016). Radio and millimeter continuum sources are also found that resemble the photo-evaporative flows from protoplanetary disks (Yusef-Zadeh et al. 2015b, 2016, 2017) seen in the Orion and Trifid nebulae (Reipurth et al. 1998), along with water and methanol masers (Wardle & Yusef-Zadeh 2008; Yusef-Zadeh et al. 2015c), and SiO (5-4) emission with luminosities and line widths matching those seen in jets from young stars in molecular clouds in the Galactic disk (Yusef-Zadeh et al. 2013, 2015b). However, none of these are regarded as conclusive, because conditions at the Galactic center make it difficult to distinguish dust-enshrouded high-mass YSOs from dusty evolved stars or low-mass YSOs from starless dusty cores (Fritz et al. 2010; Gillessen et al. 2012; Eckart et al. 2013). Furthermore, the physical and chemical conditions that create masers and SiO emission could plausibly arise in colliding flows in the complex of gas orbiting Sgr A* rather than in shock waves driven by outflows from YSOs.

Here, we report the discovery of a population of bipolar outflows, an unambiguous signature of young protostars within 0.8 parsec (pc) of Sgr A*.

2. Data Reduction and Results

Deep observations were carried out with Atacama Large Millimeter/submillimeter Array (ALMA) with high spectral resolution, spatial resolution and sensitivity to image ^{13}CO (J=2–1) and SiO (5–4) molecular lines and, in one instance, the H30 α radio recombination

line (RRL) of hydrogen in the inner pc of the Galaxy. To image ^{13}CO (2-1), H30 α RRL and SiO (5-4) emission at 220.398, 231.901, 217.105 GHz respectively, we used calibrated Band 6 archival data with a single $\sim 26''$ field of view in Cycle 3 (project code 2015.A.00021.S) observed on July 12/13, 2016.

We imaged the ALMA continuum data after self-calibration, using CASA version 4.7.2. After all spectral windows were combined, phase self-calibration solutions were derived and subsequently applied for three solution intervals: scan length, 30.25 seconds, and the integration time. In addition, a phase and amplitude self-calibration solution for an interval equal to the integration time was applied. After continuum subtraction, these phase and amplitude solutions were transferred to the ^{13}CO and H30 α line spectral window with spectral resolutions of 1.33 and 1.26 km s $^{-1}$, respectively. For the final line imaging, we combined data taken in both days and used Briggs’s weighting with robust parameters of 0.5 and 2, giving spatial resolutions of $0.49'' \times 0.39''$ (PA=-68.9 $^\circ$) and $0.51'' \times 0.39''$ (PA=-79.9 $^\circ$), respectively. Briggs parameters of 2 and 0.5 are used to weigh the uv data (Briggs et al. 1999). Briggs value of 2 (0.5) is closer to natural (uniform) weighting and more sensitive to extended (compact) features. We imaged the spectral line data cubes with channel widths of 1.33 and 1 km s $^{-1}$, respectively. We also used archival and published HCN (1-0) (Christopher et al. 2005) data with spatial (spectral) resolutions of $5.1 \times 2.7''$ (7.2 km s $^{-1}$), CS (5-4) and SiO (6-5) data with $0.76'' \times 0.59''$ (18.75 km s $^{-1}$) resolution.

We identified eleven sources with physical characteristics (size, mass, age, energetics) of young star formation activity within 0.8 pc of the black hole. The integrated flux density, angular size and position angle (PA) of individual sources are listed in Table 1a and our estimates of physical parameters are given in Table 1b. One object, Bipolar 1 (BP1), with compact bipolar CO-emission lies at a projected distance of ~ 0.6 pc (15.2 $''$) SW of Sgr A*, as shown in Figure 1a. The NW and SE lobes are blue- and red-shifted by ~ 2 km s $^{-1}$ with respect to each other, connected by intermediate velocity gas at +113 km s $^{-1}$ (green). The axis of this feature has a PA of $-42^\circ.1$, and resembles a jet connecting the two lobes. The centroids of the lobes of BP1 are separated by $\sim 1.45''$, equivalent to $\sim 1.2 \times 10^4$ AU at the 8 kpc distance of the Galactic center. The ^{13}CO lobes likely arise from the material swept up by a jet driven outflow from a central young stellar object. The total mass swept up in the NW and SE lobes is estimated to be ~ 0.19 and $0.12 M_\odot$, respectively. The equivalent momentum deposition rates are ~ 1180 and $820 L_\odot$, respectively, consistent with an outflow arising from a low mass protostar.

BP1 should therefore be embedded in a molecular cloud. A CS (5-4) line intensity map is presented in Figure 1b, taken from an ALMA observation (Moser et al. 2017), which identifies a dense and filamentary molecular cloud with narrow linewidths within $0.5''$ of BP1 at a velocity of 103 km s $^{-1}$ with a linewidth of 18.75 km s $^{-1}$. CS (5-4) has a high critical density of 5.4×10^6 cm $^{-3}$ suggesting a dense cloud, most likely the parent cloud from which the CO lobes have been swept by BP1’s protostellar jet (see below other tracers of the parent cloud). Figure 1c shows contours of ^{13}CO emission between +110 and +118 km s $^{-1}$. The blue lobe has a dominant central maximum and is elongated along the symmetry axis, as expected of a bipolar molecular outflow.

Additional evidence of a molecular cloud near BP1 can be found in Figures 1e,f,g showing a grayscale ^{13}CO line intensity between 106 and 114 km s^{-1} , a color image between +110 and +117 km s^{-1} and grayscale contours of HCN (1-0) emission between +110 and +118 km s^{-1} , respectively. The systemic velocity of BP1 is similar to those shown in these figures suggesting that the parent cloud is associated with the inner edge of the ring orbiting Sgr A*.

The interferometric HCN, CO and CS data suffer from the lack of short UV spacings, thus diffuse, extended and low density molecular emission is filtered out. In addition, the inner region of the molecular ring is traced by ionized gas associated with the mini-spiral. Absorption of molecular gas against the associated radio continuum is significant in the inner region (Marr et al. 1992). In spite of these limitations, there is clear evidence that BP1 is embedded within the inner edge of the molecular ring and is generated by a jet pushing on the surrounding molecular material. BP1 lies at the edge of a long filamentary structure (see Fig. 1e) at the interface of the molecular ring and the Western Arc, a layer of ionized gas and dusty material at a velocity of between +70 and +90 km s^{-1} .

We also detect a faint unresolved compact continuum source (BP1-226GHz) at 226 GHz between the two lobes at 0.74 ± 0.19 mJy with a resolution of $0.48'' \times 0.38''$ at $\alpha, \delta(J2000) = 17^h 45^m 38^s.923, -29^\circ 00' 30''.604$. BP1-226GHz is likely to be thermal dust emission associated with the disk of the protostar driving the outflow (see Fig. 1h). The disk mass, assuming a dust temperature of 50 K, and dust opacity $\kappa_\nu = 0.068 \text{ cm}^2 \text{ g}^{-1}$ is $\sim 0.05 M_\odot$. In addition, we find a $3.6\mu\text{m}$ source very close to the position of the 226 GHz source, as shown by a circle in Figure 1h. The relative displacement of the IR source may simply reflect the astrometric errors in aligning ALMA and VLT images as these were taken six years apart (S. Gillessen, private communication). We tentatively detect a possible counterpart to BP1 at longer IR wavelengths (N band). Future study of this source including its proper motion is needed to confirm the association of the mid-IR source with the 226 GHz continuum source.

Evolved stars also drive outflows, but they are generally isotropic because of the relatively low specific angular momentum of stellar rotation. In protoplanetary nebulae and related systems, a central binary provides orbital angular momentum and powers collimated outflows. However, these tend to have rather more extreme velocities (Sahai et al. 2017) and are traced by ionized gas.

Another bipolar source (BP2) is shown in Figure 2a with contours of blue and red-shifted ^{13}CO emission from two lobes and a third source to the north. These sources are shown superimposed on a grayscale 34 GHz continuum image (Yusef-Zadeh et al. 2015a). The region where the bipolar source BP2 lies is surrounded by ionized features with similar radial velocities based on radio recombination line observations (see Fig. 2a). Figure 2b shows the distribution of CS (5-4) emission adjacent to the source. The presence of very dense gas at a similar velocity to the lobes indicate that BP2 is associated with a dense cloud traced by CS (5-4) emission. Figure 2c shows the CO emission arising from velocities between 91-102 km s^{-1} in 16 adjacent channel maps. There are three velocity components located to the west of the N arm of the ionized mini-spiral and the parent CS cloud. There is some mixing of blue and red-shifted velocity components as shown in the southern lobes. The peak emission from blue and red-shifted lobes show a velocity difference of 4 km s^{-1} with respect to each

other centered at 97 km s^{-1} and the lobe’s centroids are spatially separated by $\sim 1''.29$. The position-velocity diagram of the lobes along a cut that passes through the peaks of blue and red-shifted components is shown in Figure 2d. The continuous velocity gradient, $\sim 3 \text{ km s}^{-1} \text{ arcsecond}^{-1}$ suggests that the blue and red-shifted components are associated. The velocity and spatial distributions suggests that the overlapping velocity components represent a bipolar outflow with the red-shifted component dominating the emission. A faint velocity component, $1.5''$ NE of the red-shifted component, has a peak velocity of 95 km s^{-1} and appears as a distinct source. It is possible that this velocity component is another bipolar outflow source that is spatially and kinematically unresolved.

The remaining nine BP sources, BP3 to BP11, are displayed in Figure 3a-i, respectively. Briefly, all sources show two lobes of emission with receding and approaching velocities, some coincide with a peak in CS (5-4) emission, giving a molecular core mass of $\sim 1 M_{\odot}$ (BP2, BP6, BP9) if we assume that the gas density is the critical density of CS (5-4) line emission, $2 \times 10^7 \text{ cm}^{-3}$, some others, e.g., BP3, show multiple transitions of SiO emission with a jet-like morphology. The SiO (8-7) emission from BP3 requires a critical density of $2 \times 10^7 \text{ cm}^{-3}$ (BP3) suggesting a highly compressed jet-like molecular material by protostellar outflows. Some sources coincide with a 226 GHz continuum source, tracing a protostellar disk (BP8) or with infrared excess sources with SEDs that are consistent with those of young stellar objects (BP3, BP4) and some show irradiated lobes of ionized gas by the external radiation field of the Galactic center (BP7, BP8).

Figure 4a shows the positions and elongated axis position angles of all eleven sources superimposed on an image of ^{13}CO emission. The red and blue colors represent the red- and blue-shifted CO emission, respectively, excluding velocities between -50 and 50 km s^{-1} . It is clear that the molecular gas in the ring and its interior provides a reservoir of molecular gas to explain the origin of the bipolar outflow sources. CO emission from the interior of the molecular gas is consistent with recent measurements (Montero-Castaño et al. 2009; Moser et al. 2017), suggesting dense molecular gas self-shields itself against strong ionizing radiation from massive stars. Evidence for dense molecular gas inside the molecular ring is also viewed in the color image of Figure 4b, which shows CO emission between -250 and $+250 \text{ km s}^{-1}$. It is clear that ^{13}CO emission fills the interior of the molecular ring in contrast to the long held view that the central cavity inside the molecular ring is devoid of any molecular gas (Christopher et al. 2005; Herrnstein & Ho 2005).

3. Discussion

Overall, the population of outflow sources presented here constitutes overwhelming evidence that star formation is taking place in clouds near the black hole despite the disruptive effect of its strong tidal field. Squeezing of clouds by the black hole’s strong tides can contribute to the collapse of clouds (Jalali et al. 2014) as well as high interstellar pressure in the inner few pc of the galaxy, $\sim 2 \times 10^9 \text{ K cm}^{-3}$ stabilizes the progenitor clouds against disruption. However, they are rendered gravitationally unstable when subject to pressures 1-2 orders of magnitude higher associated with a triggering event such as collision with the gas of the

minispiral, a high ram pressure of an approaching cloud toward Sgr A* or a jet emerging from Sgr A* (Yusef-Zadeh & Wardle 2017); Wardle and Yusef-Zadeh 2017, in preparation). Both the ionized and molecular gas in the ring and the mini-spiral provide strong external pressure against molecular cores and trigger star formation.

The mass of the individual outflow lobes is estimated by assuming that ^{13}CO emission is optically thin and is in LTE with $T \sim 100 - 300$ K. The estimated dynamical ages and momentum transfer rates depend on the unknown inclinations of the outflows with respect to the line of sight. We account for this by assuming that the intrinsic distribution of outflow axis orientation in three dimensions is isotropic. This allows us to estimate the mean dynamical age of the population as $6.5_{-3.6}^{+8.1} \times 10^3$ years (95% confidence interval), somewhat shorter than the orbital period around Sgr A*, $17000 (r/0.5\text{pc})^{1.5}$ years where r is the distance from Sgr A*. The estimated masses and momentum transfer rates are consistent with young protostellar outflows found throughout the disk of the Galaxy (Dunham et al. 2014).

The distribution of the outflow axis orientations from all 11 sources is shown as line segments on Figure 4a. The observed and derived properties of individual sources are listed in Table 1a,b. We note that the outflow sources are generally surrounded by ionized and molecular gas and located within ~ 1 pc of Sgr A*. Individual maps of CS (5-4) emission shows that seven of the 11 outflow sources are associated with molecular clouds. In spite of the low spectral resolution of CS data, the molecular core coincides with the outflow source and there is nearby dense gas that is swept by the jet from the protostar in almost all of the observed sources described here. In addition, out of 11 sources, the outflow axes of six sources are within a cone that passes through Sgr A* with PAs between 26° and 63° . It is suggestive that there is anisotropy in the distribution of outflows sources. However, this anisotropy is not significant statistically. Kuipers’s test applied to the distribution of PAs shows no statistical significance because of the small sample size. Confirmation of this correlation has to await for a larger sample of sources. If the distribution were anisotropic, large scale magnetic field in the interior of the molecular ring and the mini-spiral or a large-scale collimated outflow from Sgr A* compressing gas clouds could be responsible. We note a number of cometary radio and infrared sources, elongated nonthermal radio continuum features at a $\text{PA} \sim 50 - 60^\circ$ (Muzić et al. 2007, 2010; Yusef-Zadeh et al. 2012; Yusef-Zadeh et al. 2016). These features are interpreted as interaction sites of a collimated mildly relativistic jet from Sgr A* with the atmosphere of stars and the nonthermal Sgr A East shell. An independent set of polarization measurements at near-IR (Shahzamanian et al. 2015) shows that the position angle of Sgr A* varies over a range within the cone where most bipolar sources are detected. This distribution is consistent with a collimated outflow producing head-tail sources and possibly compressing gas, thus inducing star formation along the direction where most bipolar outflows have been detected.

Notably, detection of bipolar flows is the only means to identify low-mass YSOs, which are otherwise too faint to be detected given the 30 magnitudes of foreground visual extinction and 8 kpc distance to the Galactic center and in any case difficult to identify in the IR given the crowded field toward the Galactic center. Follow up observations will census the

population allowing studies of the initial mass function (IMF) and a comparison with star formations in less extreme environments. The 11 detected low-mass YSOs formed within the last 6500 years imply a star formation rate $\sim 5 \times 10^{-4} M_{\odot} \text{yr}^{-1}$ assuming a mean stellar mass of $\sim 0.3 M_{\odot}$. The rate would be higher if the mean mass is larger. If this is reflective of the mean rate of low-mass star formation over the past few billion years then this mode of star formation contributes significantly to the stellar mass budget in the central few pc of the Galaxy.

Our detection of bipolar sources in this apparently hostile environment suggests that star formation activity might also be higher than expected in the central molecular zone within the inner few hundred pc of the Galaxy; further searches should reveal the extent and distribution of star formation there. The measurement presented here shows that the central cavity of the molecular ring is not only filled with ionized gas but also with dense molecular gas, providing fuel for star formation (Yusef-Zadeh et al. 2013; Tsuboi et al. 2016; Moser et al. 2017). Future ALMA observations provide prospects for characterizing the gas properties inside the molecular ring. A census of low-mass star formation at the Galactic center will provide a more accurate estimate of star formation rate and the IMF near supermassive black holes. Follow up observations will characterize the population of outflows, allowing studies of the initial mass function (IMF) and a comparison with star formation in less extreme environments. This perspective is critical for understanding star formation occurring in the center of external galaxies that host supermassive black holes.

Acknowledgements This work is partially supported by the grant AST-0807400 from the NSF. The National Radio Astronomy Observatory is a facility of the National Science Foundation operated under cooperative agreement by Associated Universities, Inc. This paper makes use of the following ALMA data: ADS/JAO.ALMA#2011.0.00005.SV. ALMA is a partnership of ESO (representing its member states), NSF (USA) and NINS (Japan), together with NRC (Canada), NSC and ASIAA (Taiwan), and KASI (Republic of Korea), in cooperation with the Republic of Chile. The Joint ALMA Observatory is operated by ESO, AUI/NRAO and NAOJ. We thank R. Arendt and the referees for making useful comments.

REFERENCES

- Bonnell, I. A., & Rice, W. K. M. 2008, *Science*, 321, 1060
- Briggs, D. S., Schwab, F. R., & Sramek, R. A. 1999, *Synthesis Imaging in Radio Astronomy II*, 180, 127
- Christopher, M. H., Scoville, N. Z., Stolovy, S. R., & Yun, M. S. 2005, *Astrophys. J.*, 622, 346
- Dunham, M. M., Arce, H. G., Mardones, D., et al. 2014, *ApJ*, 783, 29
- Eckart, A., Moutaka, J., Viehmann, T., Straubmeier, C., & Mouawad, N. 2004, *Astrophys. J.*, 602, 760

- Eckart, A., Mu Vzić, K., Yazici, S., et al. 2013, *Astron. Astrophys.*, 551, A18
- Fritz, T. K., Gillessen, S., Dodds-Eden, K., et al. 2010, *Astrophys. J.*, 721, 395
- Gillessen, S., Genzel, R., Fritz, T. K., et al. 2012, *Nature*, 481, 51
- Herrnstein, R. M., & Ho, P. T. P. 2005, *ApJ*, 620, 287
- Jalali, B., Pelupessy, F. I., Eckart, A., et al. 2014, *MNRAS*, 444, 1205
- Lu, J. R., Ghez, A. M., Hornstein, S. D., et al. 2009, *Astrophys. J.*, 690, 1463
- Marr, J. M., Rudolph, A. L., Pauls, T. A., Wright, M. C. H., & Backer, D. C. 1992, *ApJ*, 400, L29
- Mapelli, M., Hayfield, T., Mayer, L., & Wadsley, J. 2012, *Astrophys. J.*, 749, 168
- Montero-Castaño, M., Herrnstein, R. M., & Ho, P. T. P. 2009, *Astrophys. J.*, 695, 1477
- Morris, M. 1993, *Astrophys. J.*, 408, 496
- Moser, L., Sánchez-Monge, Á., Eckart, A., et al. 2017, *Astron. Astrophys.*, 603, A68
- Muzić, K., Eckart, A., Schödel, R., et al. 2010, *A&A*, 521, A13
- Muzić, K., Eckart, A., Schödel, R., Meyer, L., & Zensus, A. 2007, *A&A*, 469, 993
- Nayakshin, S., Cuadra, J., & Springel, V. 2007, *Mon. Not. R. Astron. Soc.*, 379, 21
- Paumard, T., Genzel, R., Martins, F., et al. 2006, *Astrophys. J.*, 643, 1011
- Reipurth, B., Bally, J., Fesen, R. A., & Devine, D. 1998, *Nature*, 396, 343
- Sahai, R., Vlemmings, W. H. T., Gledhill, T., et al. 2017, *Astrophys. J.*, 835, L13
- Shahzamanian, B., Eckart, A., Valencia-S., M., et al. 2015, *A&A*, 576, A20
- Tsuboi, M., Kitamura, Y., Miyoshi, M., et al. 2016, *Publ. Astron. Soc. Jpn*, 68, L7
- Viehmann, T., Eckart, A., Schödel, R., et al. 2005, *Astron. Astrophys.*, 433, 117
- Wardle, M., & Yusef-Zadeh, F. 2008, *Astrophys. J.*, 683, L37
- . 2012, *Astrophys. J.*, 750, L38
- Yoshikawa, T., Nishiyama, S., Tamura, M., Ishii, M., & Nagata, T. 2013, *Astrophys. J.*, 778, 92
- Yusef-Zadeh, F., Bushouse, H., Schödel, R., et al. 2015a, *Astrophys. J.*, 809, 10
- Yusef-Zadeh, F., Cotton, B., Wardle, M., et al. 2017, *Mon. Not. R. Astron. Soc.*, 467, 922
- Yusef-Zadeh, F., Roberts, D. A., Wardle, M., et al. 2015b, *Astrophys. J.*, 801, L26

Yusef-Zadeh, F., & Wardle, M. 2017, IAU Symposium, 324, 111

Yusef-Zadeh, F., Arendt, R., Bushouse, H., et al. 2012, ApJ, 758, L11

Yusef-Zadeh, F., Wardle, M., Schödel, R., et al. 2016, Astrophys. J., 819, 60

Yusef-Zadeh, F., Royster, M., Wardle, M., et al. 2013, Astrophys. J., 767, L32

Yusef-Zadeh, F., Wardle, M., Sewilo, M., et al. 2015c, Astrophys. J., 808, 97

Table 1: *a Top* Entries give the source name, the coordinates, the flux density, the extent of the blue- and red-shifted lobes in terms of the beam solid angle, the velocity difference of the lobes, the angular separation of the lobes in arcseconds, the center velocity and the position angle of the source in degrees. *b Bottom* Physical parameters of molecular outflows with entries giving the source name, the mass and hydrogen number density of individual lobes, the total mass of the lobes, the jet length and the outflow force.

Source	J2000 coord		Red Lobe		Blue Lobe		Δv km s ⁻¹	$\Delta\theta$ "	v_{center} km s ⁻¹	PA deg.
	RA(s)	Dec(")	F Δv mJy km s ⁻¹	Ω beam	F Δv mJy km s ⁻¹	Ω beam				
BP1	38.917	30.72	215	2.9	135	2.4	2	1.45	113.0	-42.1
BP2	40.417	15.48	1140	3.6	450	1.9	4	1.29	97.0	26.6
BP3	40.495	29.11	7.8	1.5	10.3	1.1	1	0.74	163.5	51.3
BP4	40.840	21.03	54	1.5	–	–	1	0.17	197.5	54.3
BP5	39.869	22.24	63	1.4	116	1.6	4	0.41	-93.0	-88.9
BP6	39.343	44.27	2489	6.5	1198	5.1	5	1.01	68.5	5.1
BP7	39.440	32.82	22.2	2.9	–	–	1	1.80	-199.5	56.1
BP8 _{HII}	39.638	31.28	6.2	1.2	5.1	1.1	13	0.81	-81.8	-50.7
BP9	40.414	30.41	155	2.9	510	2.1	2	3.28	-59	-50.3
BP10	39.296	29.39	171	1.2	170	1.2	3	0.44	-57	62.8
BP11	40.553	16.62	42.7	1.5	44.7	1.35	1	0.39	163.5	22.5

Source	Red Lobe		Blue Lobe		Total	jet length $\times(\sin i)$ 10 ¹⁷ cm	Force $\times(\cos^2 i / \sin i)$ L _⊙ / c
	Mass M_{\odot}	n_H cm ⁻³	Mass M_{\odot}	n_H cm ⁻³	Mass M_{\odot}		
BP1	0.19	2.6e+05	0.12	2.1e+05	0.32	0.87	5.7e+02
BP2	1.0	9.8e+05	0.41	1.0e+06	1.4	0.77	1.1e+04
BP3	0.007	2.5e+04	0.0093	5.3e+04	0.016	0.44	1.4e+01
BP4	0.049	1.7e+05	–	–	–	0.10	–
BP5	0.057	2.2e+05	0.10	3.4e+05	0.16	0.25	4.1e+03
BP6	2.2	8.9e+05	1.1	6.1e+05	3.3	0.60	5.4e+04
BP7	0.020	2.6e+04	–	–	–	1.1	–
BP8 _{HII}	0.0056	2.8e+04	0.0046	2.6e+04	0.01	0.48	1.4e+04
BP9	0.14	1.8e+05	0.46	9.9e+05	0.60	2.0	4.8e+02
BP10	0.15	7.7e+05	0.15	7.6e+05	0.31	0.26	4.1e+03
BP11	0.039	1.4e+05	0.04	1.7e+05	0.079	0.23	1.3e+02

Fig. 1.— (see Fig. 1 next page) The relative coordinates (0,0) in Figures 1-4 coincide with the position of Sgr A* at $\alpha, \delta(J2000) = 17^h 45^m 40^s.038, -29^\circ 00' 28''.069$. (a) The blue and red-shifted lobes are detected to the NE and SW and the green color represents the intermediate velocity range. The intensity range is between -1 and 10 mJy beam⁻¹. The cross coincides with the position of a compact 226 GHz source (see (h)). (b) A color image of CS(5-4) emission at a velocity of 103 km s⁻¹, channel width of 18.75 km s⁻¹ and rms noise per channel 0.9 mJy beam⁻¹. The cross is the same as in (a). (c) Contours of intensity from 9 channels at -1, 1, 2, 3, 4, 5, 6, 8, 10, 12, 14 mJy beam⁻¹ km s⁻¹ with velocities ranging between 110 and 118 km s⁻¹. A primary beam correction has not been applied. The mixing of blue and red-shifted CO emission from the two lobes is most likely due to low 1.33 km s⁻¹ spectral resolution. (d) PV diagram constructed along the axis of the symmetry of BP1 at PA $\sim -42^\circ.6$ connecting the two lobes. The color bar to the right shows the intensity of the ¹³CO emission corrected for the primary beam. (e) ¹³CO line intensity integrated over 106 and 114 km s⁻¹. (f) A true color ¹³CO image at velocities between 110-112, 113-114 and 115-117 km s⁻¹, in red, green and blue, respectively. The intensity range is between -1 and 5 mJy beam⁻¹. (g) Contours of HCN (1-0) line intensity integrated over 105 and 118 km s⁻¹ with levels (-1, -0.5, 0.5, 1,..., 3, 4,...10) $\times 0.67$ Jy km s⁻¹. This data set is taken from interferometric observations (Owens Valley Radio Observatory) with a resolution of 5.1'' \times 2.7'' (Christopher et al. 2005). (h) Contours of 226 GHz emission with a resolution of 0.42'' \times 0.33'' (PA= -74°) with levels -0.1, 0.1, 0.2, 0.3, 0.4, 0.5, 0.6 mJy are superimposed on a grayscale ¹³CO image at a velocity of 113 km s⁻¹. A 226 GHz source is detected at the center of BP1. (i) A composite image of 3.8 μ m (red) and ¹³CO at 113 km s⁻¹ (green). The black circle shows the IR source which could be the counterpart to the 226GHz continuum source seen in (h). The beam sizes of the CO and CS data are displayed on the bottom left corners of (a) and (b), respectively.

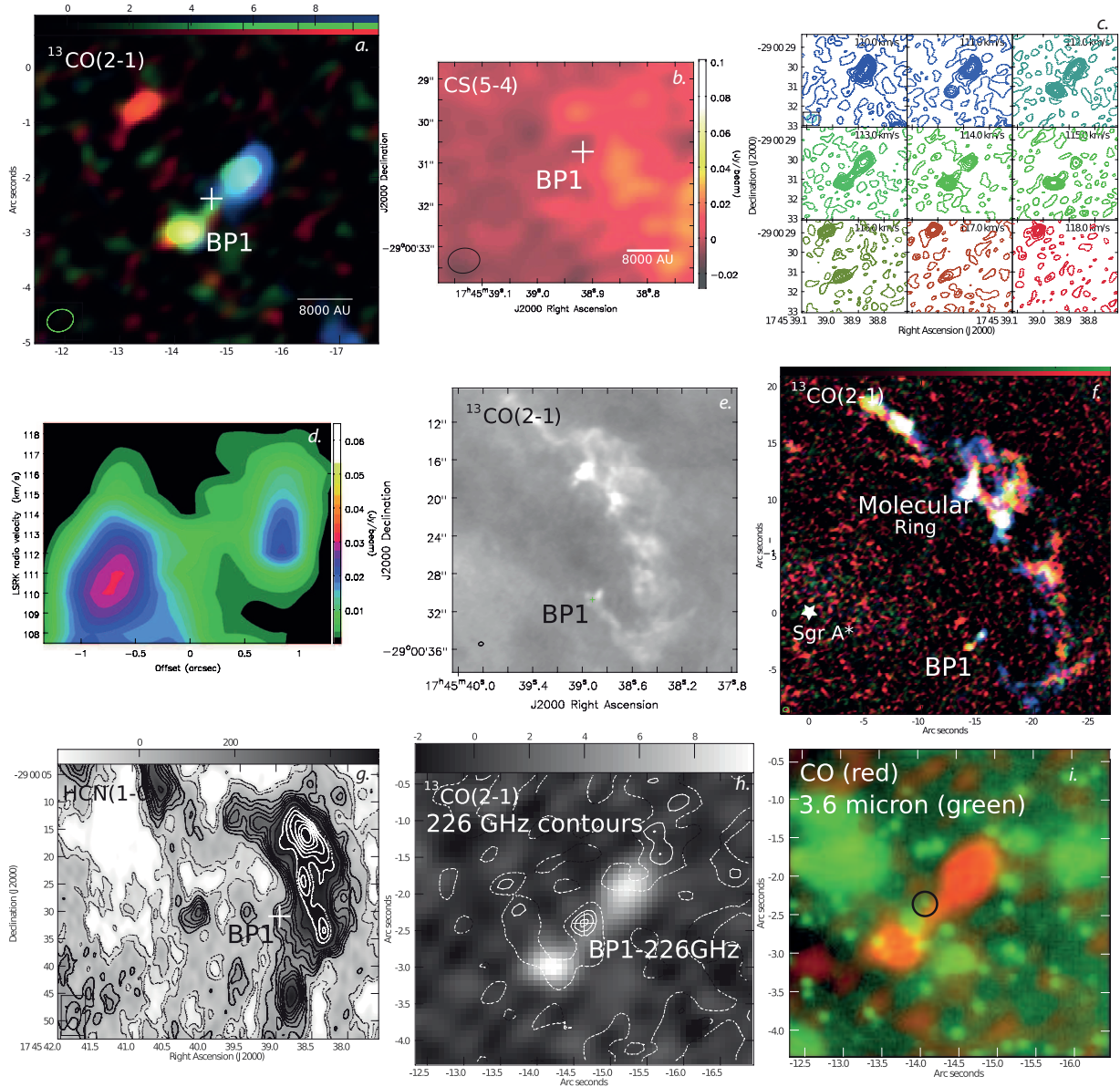


Fig. 2.— (see Fig. 2 next page) (a) Contours of integrated ^{13}CO emission between 92-96 and 97-101 km s^{-1} , shown in blue and red, respectively, at 2, 2.5, 3, 3.5, 4, 4.5, 5, 6 $\text{mJy beam}^{-1} \text{km s}^{-1}$ are superimposed on a 34 GHz grayscale image with grayscale range between -115 and 100 $\mu\text{Jy beam}^{-1}$. (b) CS(5-4) emission from a cloud centered at 84 km s^{-1} with a linewidth of 18.75 km s^{-1} . The cross shows the center of CO emission from BP1. The CS(54) rms noise per channel is 0.9 mJy beam^{-1} , (Moser et al. 2017). (c) Contours of 16 channel maps with levels set at (-1, 1, 2, 3, 4, 6, 8, 10, 14, 18, 22, 26) $\times 3 \text{ mJy beam}^{-1}$. (d) PV diagram of BP2 made with a slice at a PA= $26^\circ.56$. The beam sizes are shown in bottom left corners in (a) and (b).

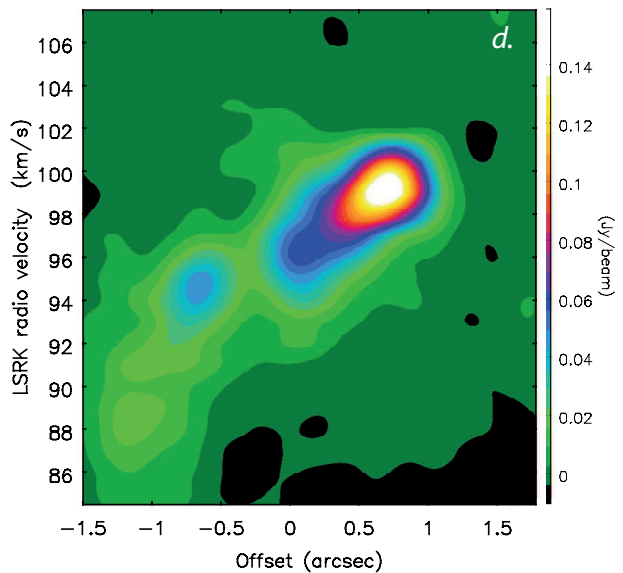
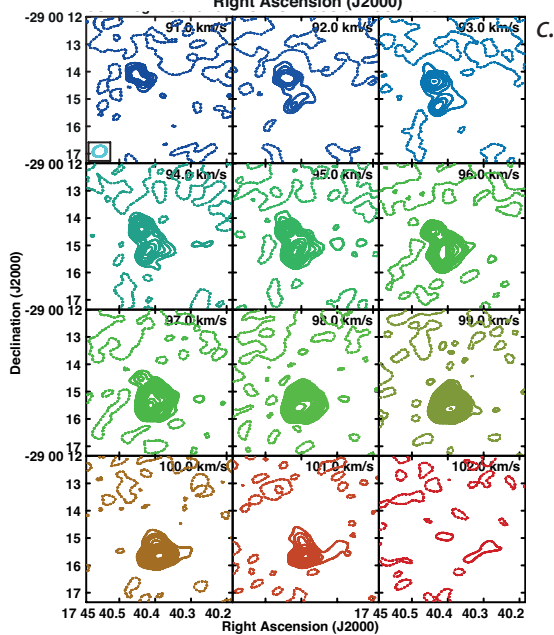
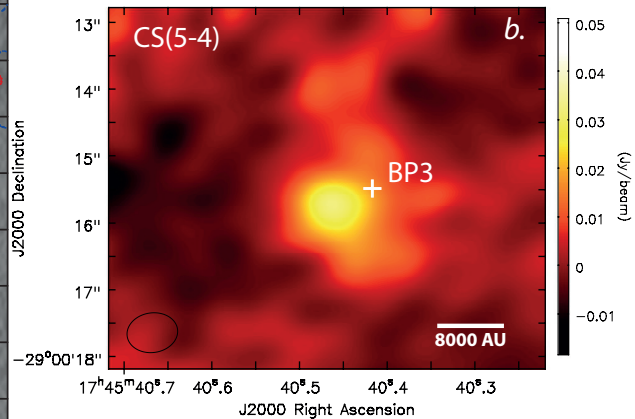
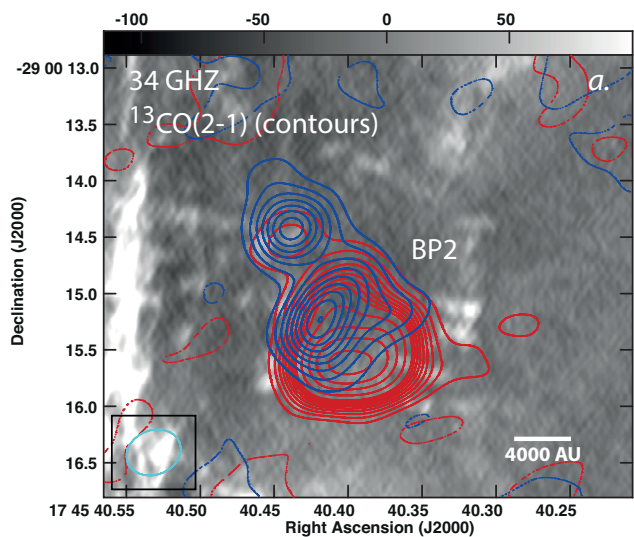


Fig. 3.— (see Fig. 3 next page) (a) A blue- and red-shifted image of BP3 corresponding to velocities 162-163 and 164-165 km s⁻¹ respectively. The integrated intensity ranges between -1 and 2.4 mJy/beam km s⁻¹. (b) Contours of red- and blue-shifted CO emission with levels set at -1.5, 1.5, 2, 2.5, 3, 4, 5 and 6 mJy beam⁻¹ km s⁻¹ at 201 and 196 km s⁻¹ respectively. (c) Contours of blue and red-shifted ¹³CO emission corresponding to velocities -96 to -94 and -92 to -90 km s⁻¹ respectively, with levels at (-0.4, 0.4, 0.5, 0.6, 0.8, 1, 1.2, 1.4, 1.6, 1.8, 2, 2.2, 2.4, 2.6, 2.8, 3) × 15 mJy km s⁻¹. The grayscale image with a range between -100 and 50 μJy beam⁻¹ shows the head-tail radio source associated with the supergiant star IRS 7 at the Galactic center. (d) Contours of blue and red-shifted ¹³CO emission corresponding to velocities 62–69 and 70–76 km s⁻¹ respectively, with levels at (-1, 1, 2, 3, 4, 5, 6) × 100 mJy km s⁻¹. The grayscale image of the blue-shifted velocities has a range between -100 and 100 μJy beam⁻¹. (e) Contours of integrated ¹³CO line intensity between -200 and -199 km s⁻¹ at -2, 2, 4, 6, 8 mJy km s⁻¹. The color image shows the ionized gas traced by H30α RRL (green) and molecular material traced by CO emission (red). The intensity ranges between -2 and 13 mJy beam⁻¹. (f) Contours of blue (-94.3 to -88 km s⁻¹) and red-shifted (-84.8 to -78.5 km s⁻¹) H30α recombination line intensity at velocities between at (-3, 3, 4, 5, 6, 7, 8, 9, 1) × 3.2 mJy km s⁻¹ with a spatial resolution of 0.46'' × 0.35''. The cross coincides with a 226 GHz continuum peak intensity 0.62 ± 0.23 mJy beam⁻¹. The integrated 226 GHz intensities from the blue and red-shifted lobes are 0.63 and 0.54 mJy integrated over 1.4 and 1.3 times the solid angle of the synthesized beam which is 0.35'' × 0.22''. (g) A grayscale image of ¹³CO emission at -56 km s⁻¹ with intensity range between -1 and 20 mJy beam⁻¹. (h) A color image of the blue- and red-shifted lobes of ¹³CO sources. Contours of red-shifted component is set at (-1, 1, 2, 4, 7, 10, 14) × 6 mJy beam⁻¹ integrated over velocities between -57 and -54 km s⁻¹. (i) Contours of blue and red-shifted ¹³CO intensity at velocities between 160 to 163 and 164 to 167 km s⁻¹ at (-3, 3, 4, 5, 6, 7, 8, 9, 10) × 5 mJy km s⁻¹ superimposed on a 34 GHz continuum image with grayscale range between -100 and 200 μJy beam⁻¹.

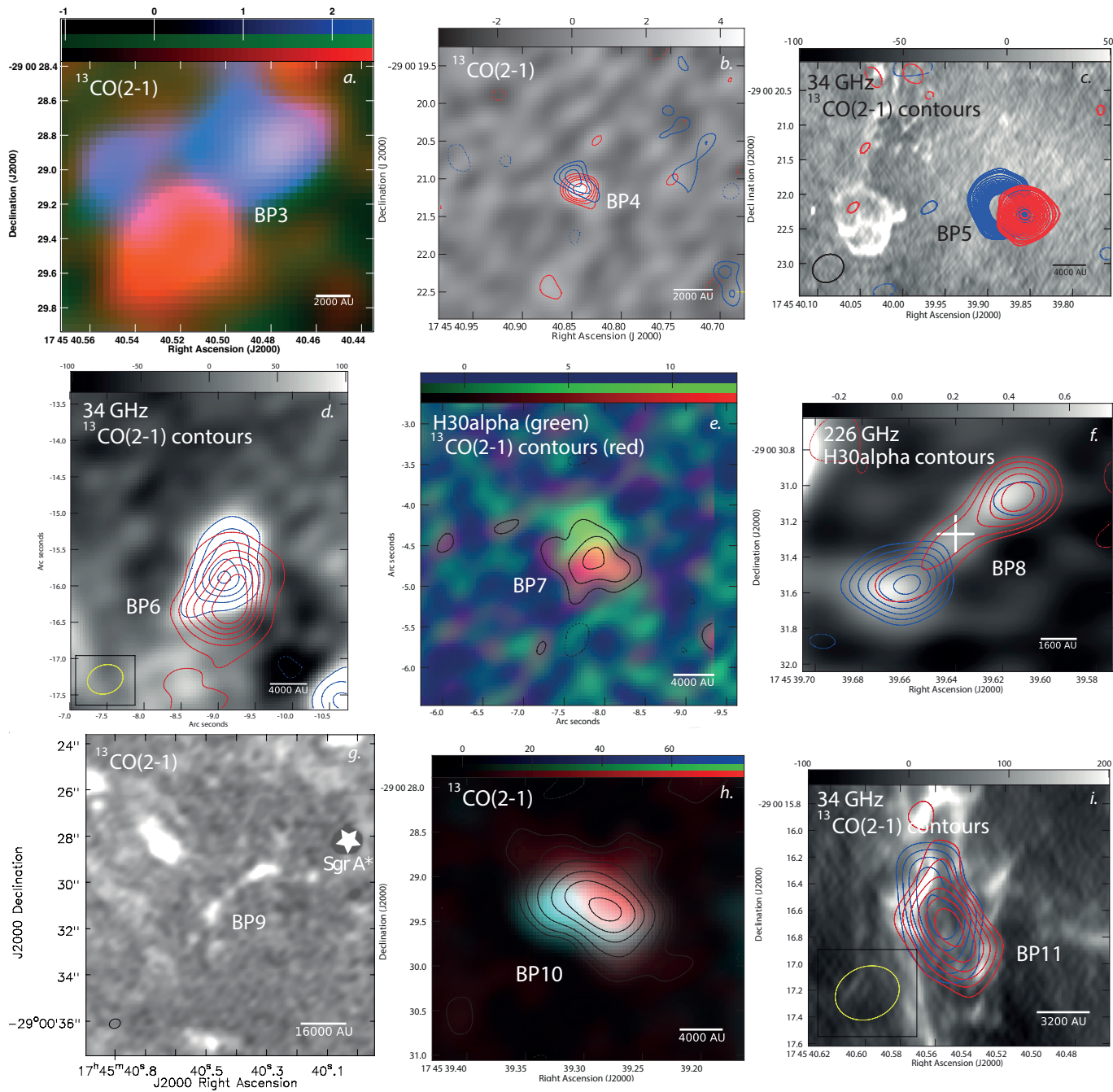


Fig. 4.— (see Fig. 4 next page) (a) The position and the PA of the symmetry axis of all eleven outflow sources are drawn as line segments and are superimposed on a color image of the distribution of ^{13}CO emission. The ^{13}CO intensity integrated from -50 to -200 km s^{-1} and 50 to 200 km s^{-1} is shown in blue and red, respectively. The image is not primary beam corrected. The flux density range is between -0.66 and 0.66 Jy km s^{-1} . The black spot coincides with the position of Sgr A*. The position angle of individual outflow source is tabulated in the last column of Table 1 and is given in degrees east of north. (b) The distribution of ^{13}CO showing peak emission at velocities ranging between -250 and 250 km s^{-1} . The ellipse outlines schematically the molecular ring detected in HCN (1-0) (Christopher et al. 2005). The images shown in (a) and (b) reveal that ^{13}CO with a wide range of velocities fills the interior of the molecular ring. The CO line intensity ranges are -0.01 to 0.1 (red), -0.01 to 0.2 (green) and -0.2 to -0.03 (blue) Jy km s^{-1} . The image is primary beam corrected.

